Sustainable Energy & Fuels

ROYAL SOCIETY OF CHEMISTRY

PAPER

View Article Online
View Journal | View Issue

Cite this: *Sustainable Energy Fuels*, 2022, **6**, 3565

Push–pull organic dyes and dye-catalyst assembly featuring a benzothiadiazole unit for photoelectrochemical hydrogen production†

A. Moinel, [ab] M. Brochnow, [a] C. Aumaître, [a] E. Giannoudis, [b] J. Fize, [b] C. Saint-Pierre, [a] J. Pécaut, [a] P. Maldivi, [a] V. Artero, [b] R. Demadrille *[a] and M. Chavarot-Kerlidou *[b]

In this work, we report the design and the preparation of two new dyes and a molecular dyad for the photoelectrochemical hydrogen production from water in a dye-sensitized photoelectrochemical cell (DSPEC). We designed dyes that include a benzothiadiazole (BTD) and an indacenodithiophene (IDT) units, and we obtained a new molecular dyad by covalent coupling with the cobalt diimine–dioxime catalyst. The introduction of the benzothiadiazole core in the structure improves the absorption properties and leads to an extension of the spectrum in the visible range up to 650 nm. The photoelectrochemical properties of the new dyad were evaluated on pristine and lithium-doped NiO electrodes. We demonstrate that increasing the light harvesting efficiency of the dyad by introducing a IDT–BTD chromophore is clearly beneficial for the photoelectrochemical activity. We also demonstrate that lithium doping of NiO, which improves the electronic conductivity of the mesoporous film, leads to a significant increase in performance, in terms of TON and F.E., more than doubled with our new dyad. This BTD-based molecular system outperforms the results of previously reported dyads using the same catalyst.

Received 3rd March 2022
Accepted 9th June 2022

DOI: 10.1039/d2se00292b

rsc.li/sustainable-energy

1 Introduction

Over the last decade, Dye-Sensitized Photoelectrochemical Cells (DSPECs) have gathered an increasing interest due to their ability to produce hydrogen (H_2) through light-driven water splitting.[1,2] Using this concept, Sun and coworkers reported the first Pt-free tandem photoelectrochemical cells by taking advantage of molecular catalysts to drive the two redox half-reactions – namely water oxidation at the photoanode and proton reduction at the photocathode – that take place into separated compartments.[3,4] A key advantage of DSPECs also relies on the possibility to use dyes whose absorption properties can be easily tuned to efficiently harvest photons from the visible range of the solar spectrum, with the photoactive ruthenium polypyridyl complexes being vastly employed both at the photoanode[5] and photocathode[6,7] sides. However, as for Dye-Sensitized Solar Cells (DSSCs), the low natural abundance of this element, the moderate visible light absorption of ruthenium-complexes and their plausible toxicity are severe constraints that will prevent their wide use. Metal-free organic dyes are appealing alternatives to ruthenium in that context. They contain only abundant elements and can thus be prepared at lower cost. Their optoelectronic properties can be quite easily adjusted by engineering of their molecular structure, and they usually demonstrate a high molar absorption coefficient in the visible region, allowing reducing the thickness of the semi-conducting mesoporous films onto which they are attached without reducing the light harvesting efficiency.[8]

Several examples of functional H_2-evolving photocathodes integrating porphyrins,[9,10] coumarin,[11] diketopyrrolopyrrole-[12,13] or perylene monoimide-based[14] dyes and push–pull structures embedding various chromophores[4,15–22] have been described in the literature. However, there are no clear structure–property relationships for most of these dyes and design rules are still lacking in this area. In 2016, we reported the first example of a noble metal-free dye-sensitized NiO photocathode featuring an organic push–pull dye (**T1**) covalently linked to the cobalt-diimine–dioxime H_2-evolving catalyst (**T1-Co** in Fig. 1).[17] Such a construction should favor unidirectional electron transfer from the valence band of the semi-conductor to the catalytic center, and is expected to slow down recombination processes through increased spatial charge separation. However, with a single thiophene unit in the push–pull structure, **T1** exhibits relatively low visible light absorption and a poor charge

[a]*Univ. Grenoble Alpes, CNRS, CEA, IRIG, SyMMES, 17 rue des martyrs, 38000 Grenoble, France. E-mail: renaud.demadrille@cea.fr*

[b]*Univ. Grenoble Alpes, CNRS, CEA, IRIG, Laboratoire de Chimie et Biologie des Métaux, 17 rue des Martyrs, F-38000 Grenoble, France. E-mail: murielle.chavarot-kerlidou@cea.fr*

† Electronic supplementary information (ESI) available. See https://doi.org/10.1039/d2se00292b

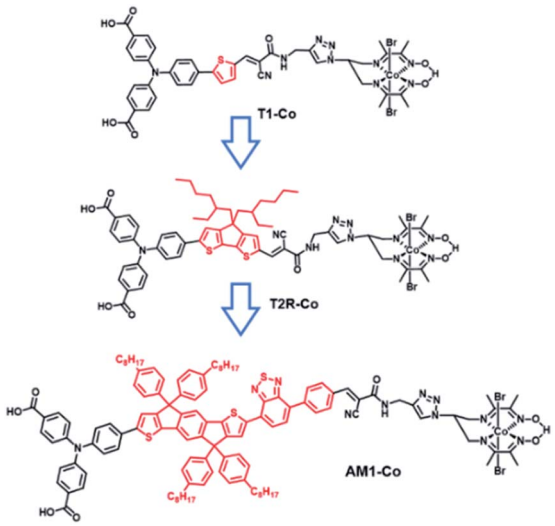

Fig. 1 Chemical structures of T1-Co and T2R-Co dyads used as reference, and AM1-Co synthesized in this work.

separation efficiency. An optimization of the system was proposed with the introduction of a cyclopenta[1,2-*b*:5,4-*b*′] dithiophene (CPDT) bridge (**T2R-Co** in Fig. 1).[23] Using a standardized protocol, we were able to compare the photoelectrochemical performances of the different dyads and to demonstrate superior performances with **T2R-Co**.

In the last years, new organic dyes were disclosed in the field of DSSCs and some of them are very efficient photosensitizers. They could be a source of inspiration for the development of molecular dyads with improved photocatalytic activity. When analyzing the chemical structures of some of the most efficient organic dyes reported in DSSCs,[24–28] it appears that a benzothiadiazole (BTD) unit is often used as a building block.[7,29] However, surprisingly, this motif has rarely been considered for the preparation of dyes applicable in photocatalysis[30] or DSPECs.[31] BTD is an electron-deficient unit, widely used in the synthesis of dyes for DSSCs, since it increases the push–pull effect in the dye structure, thus shifting the internal charge transfer (ICT) absorption band towards longer wavelengths and improving the spatial separation of HOMO and LUMO orbitals.[32,33]

In this work, our goal was to evaluate the potential of the IDT–BTD chromophore for the preparation of dye-catalysts assemblies specifically designed for photoelectrochemical hydrogen production. To this purpose, we embedded a benzothiadiazole unit in a D–π–A type chemical structure, and the resulting dye was later covalently assembled with the hydrogen-evolving cobalt diimine dioxime catalyst. We investigated the structural and optoelectronic properties of the new dye and dyad that both show a shift of their absorption spectra towards longer wavelengths compared to the previously reported systems.

Then, the photocathodes were fabricated by grafting the dye or the dyad onto NiO mesoporous thin films. Two types of NiO electrodes were used in this work, pristine ones or Li-doped ones. Then, their photoelectrochemical activity for hydrogen production was studied. We demonstrate that the novel dyad, embedding an indacenodithiophene (IDT) unit coupled to a BTD, shows a higher efficiency compared to the dyads based on the same catalytic system, **T1-Co** and **T2R-Co** (see Fig. 1).[23] We also show that Li-doped electrodes help to improve the steady-state photocurrent density and therefore the turnover number of this new molecular system.

2 Results and discussion

2.1. Design and synthesis

With the goal to obtain a new molecular system suitable to fabricate a photocathode on NiO film, we designed a push–pull type molecular architecture with the BTD unit at its core. An electron-donating group was connected *via* a π-conjugated spacer on one side and an electron-withdrawing group on the other side bearing an alkyne function allowing the coupling of the catalytic center. With the goal to compare our new molecule with **T1** and **T2R** reference dyes, we kept both ends identical. A triphenylamine (TPA) was used as electron-donor moiety bearing the anchoring carboxylic acid functions. A cyanoacrylamide was employed as part of the electron-withdrawing moiety bearing an alkyne function to covalently link the H_2-evolving catalyst.

A review of the literature on dyes for DSSCs incorporating a BTD unit indicates that these dyes have a higher propensity to aggregate after grafting.[34,35] To avoid this phenomenon we decided to use an indacenodithiophene (IDT) spacer to connect the TPA bearing the anchor functions to the BTD unit. The presence of 4-phenyloctyl substituents on the IDT bridge decreases the aggregation and increases the solubility.[36] Besides, the presence of 4-phenyloctyl substituents is expected to create a hydrophobic barrier at the surface of the p-type mesoporous oxide material, protecting the anchoring functions from hydrolysis and thus, preventing desorption of the molecular dyad from the electrode surface.[18] Another advantage of such unit is the good delocalization of the π-conjugated system through this block leading to an extension of the absorption in the UV domain of the final system (Fig. 1).

In this work, in addition to the dyad, two dyes were designed *i.e.* **$^{t\mathrm{Bu}}$AM1-alkyne** and **$^{t\mathrm{Bu}}$AM1-OMe**. Their molecular structures were investigated by DFT computations, using the ADF 2016 package.[37,38] Geometry optimizations were carried out with the GGA revBPE functional. They were followed by single points in a continuum model for H_2O, using the hybrid B3LYP functional, in order to provide the energy level and the spatial organization of charges of the frontier orbitals (see ESI† for computational details). As shown in ESI (Table S1†), the HOMO and LUMO orbitals are spatially well localized, allowing a directional charge separation upon irradiation of the dye. Besides, the HOMO level is found at −5.08 eV whereas the LUMO energy levels lies at −3.03 eV. Therefore, the predicted energy levels of the HOMO and the LUMO comply with the required thermodynamics for hydrogen evolution application, *i.e.* the HOMO orbital is lower than the NiO valence band and the LUMO orbital higher than the Co(II)/Co(I) redox couple (Fig. S1†). The energy level of Co(II)/Co(I) redox couple in our

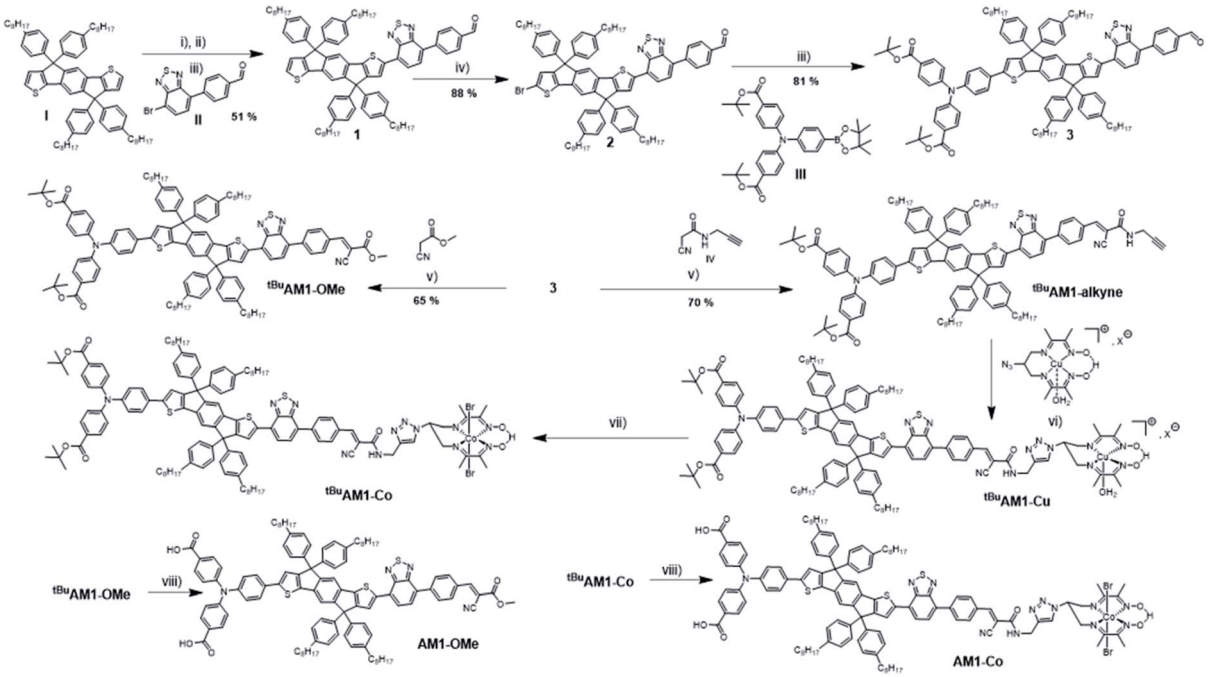

Fig. 2 Synthetic routes and intermediates towards **AM1-alkyne** and **AM1-OMe** dyes and **AM1-Co** dyad, conditions: (i) *n*-BuLi, THF, −78 °C, 1 h; (ii) ^{i}PrO-Bpin, THF, RT, 2 h; (iii) Pd_2dba_3, $HPtBu_3BF_4$, K_3PO_4, THF/H_2O, 40 °C, 16 h; (iv) NBS, THF/DMF, dark, 25 °C, 16 h; (v) NH_4OAc, toluene, 90 °C, 3 days; (vi) $CuSO_4$, NaAsc, H_2O/CH_2Cl_2/MeOH, 25 °C, 24 h; (vii) $CoBr_2 \cdot H_2O$, O_2, acetone, 25 °C, 12 h; (viii) TFA, DCM, 25 °C, 6 h.

system was first considered as similar to **T1-Co** and **T2R-Co**, but was accurately measured by cyclic voltammetry afterwards. It is important to note that when the BTD is not present in the **^{tBu}AM1-alkyne** structure, theoretical calculations show that the absorption range is significantly reduced (see Table S1 and Fig. S2†), which confirms the relevance of using the BTD unit in the dyad structure.

The synthetic route towards the dyes and the molecular dyad is reported in Fig. 2; it relies on four previously reported building blocks *i.e.* IDT (**I**),[39] BTD (**II**),[40] TPA (**III**)[41] and CN-Alc (**IV**).[42] First, we performed the dissymetrization of the IDT (**I**) through functionalization using one equivalent of *n*-butyl lithium followed by the addition of one equivalent of 2-isopropoxy-4,4,5,5-tetramethyl-1,3,2-dioxoborolane. The resulting boronic ester product was directly involved in a Suzuki–Miyaura cross-coupling reaction with the BTD (**II**) unit to yield compound **1** with 51% yield. Product **2** was obtained in high yield *via* a selective bromination of the product **1** with *N*-bromosuccinimide. The second Suzuki–Miyaura cross-coupling reaction between **2** and the TPA (**III**) yielded the product **3** in good yields. From there, Knoevenagel condensation reactions were run between the aldehyde **3** and either precursor **IV** or the methyl-cyanoacrylic ester to yield target compounds **^{tBu}AM1-alkyne** and **^{tBu}AM1-OMe** respectively (Fig. S3 and S4†). **^{tBu}AM1-OMe** was synthesized to be a reference compound for opto-electrochemical and photo-electrochemical activity studies.

The copper diimine–dioxime catalyst precursor [Cu(DO)(DOH)N_3pn(OH_2)](ClO_4) was assembled with **^{tBu}AM1-alkyne** using a copper-catalyzed azide–alkyne cycloaddition (CuAAC) procedure, followed by a transmetallation step with $CoBr_2$ under air bubbling to obtain the stable diamagnetic Co(III) complex **^{tBu}AM1-Co**, according to our previously reported procedure.[17] The formation of the pseudo-macrocyclic Co(DO)(DOH)pn moiety in **^{tBu}AM1-Co** was confirmed by ^{1}H NMR analysis, with the characteristic signal of the bridging proton observed at 19.36 ppm (Fig. S5†) and MALDI-ToF-MS analysis.

In the last step, the carboxylic acid anchoring functions are recovered through hydrolysis of the *tert*-butylester groups under mild conditions using TFA. Detailed procedures and characterizations (Fig. S6 and S7) are given in the ESI.†

2.2 Opto-electronic properties

The UV-Vis absorption spectra of the dyes **^{tBu}AM1-alkyne** and **^{tBu}AM1-OMe** were recorded in DCM at 25 °C and compared to the ones of **^{tBu}T1** and **^{tBu}T2R**. The optical and electronic properties of all compounds are gathered in Table 1. In Fig. 3, **^{tBu}AM1-alkyne** and **^{tBu}AM1-OMe** exhibit almost identical absorption spectra with two absorption peaks centered at 360 nm and 405 nm in the UV region. These bands are originating from π–π* transition whereas the broad absorption band located in the visible range at around 524 nm can be attributed to an ICT transition.[40] For the ICT band, this corresponds to a bathochromic shift of around 75 nm compared to the reference dye **^{tBu}T1**, and 56 nm when compared to **^{tBu}T2R** dye. As we expected, the addition of the IDT unit enlarges and increases the absorption in the UV region while the ICT band extend the absorption towards longer wavelengths in the visible region. **^{tBu}AM1-alkyne** and **^{tBu}AM1-OMe** exhibit molar extinction coefficients almost twice as much as the reference dyes in the UV range. Despite lower absorption coefficient for the ICT

Table 1 Selected optical and electronic properties of the dyes ^{tBu}AM1-OMe, ^{tBu}AM1-alkyne, the catalyst Co and the dyad ^{tBu}AM1-Co

Compound	λ_1[a] (nm) ε_1 (M^{-1} cm^{-1})	λ_2[a] (nm) ε_2 (M^{-1} cm^{-1})	λ_{em}[a] emission	E_{0-0}[b]	Dye^+/Dye[c] (V *vs.* $Fc^{+/0}$)	Dye^{2+}/Dye^+[c] (V *vs.* $Fc^{+/0}$)	Dye/Dye^-[d] (V *vs.* $Fc^{+/0}$)	Co(II)/Co(I)[d] (V *vs.* $Fc^{+/0}$)	Co(III)/Co(II)[d] (V *vs.* $Fc^{+/0}$)
^{tBu}AM1-OMe	405 (62 900)	524 (54 900)	717 nm	2.12 eV	0.37	0.52	−1.48[c]		
^{tBu}AM1-alkyne	404 (62 100)	523 (55 600)	716 nm	2.08 eV	0.30	0.55	−1.57		
Co								−1.18	−0.67
^{tBu}AM1-Co	406 (46 100)	514 (33 800)	718 nm	2.11 eV	0.29	0.51	−1.52	−1.12	−0.73
^{tBu}T1	352 (38 600)	450 (39 500)	653 nm[e]		0.68[f]		−1.64[f]		
^{tBu}T2R	356 (33 800)	506 (64 200)	674 nm[g]		0.48[g]		−1.57[g]		
^{tBu}T1-Co	349 (33 600)[f]	431 (31 800)[f]	630 nm[e]		0.68[f]		−1.64[f]	−1.02[f]	−0.55[f]
^{tBu}T2R-Co	353 (32 800)[g]	490 (57 900)[g]	663 nm[g]		0.45[g]		−1.67[g]	−1.02[g]	−0.53[g]

[a] In solution (DCM, 10^{-5} M). [b] Calculated from absorption and emission spectra reported in Fig. S8 and the equation $E = 1241/\lambda_{0-0}$. Potentials measured *vs.* $Fc^{+/0}$ at 25 °C in a solution of $n$$Bu_4NPF_6$ 0.1 M in DCM. [c] Or DMF. [d] As supporting electrolyte with a scan rate of 50 mV s^{-1}. [e] Reported in ACN.[43] [f] Reported in ACN for UV-Vis and in DMF for electrochemistry.[17] [g] Reported in ACN for UV-Vis and in DMF for electrochemistry.[44]

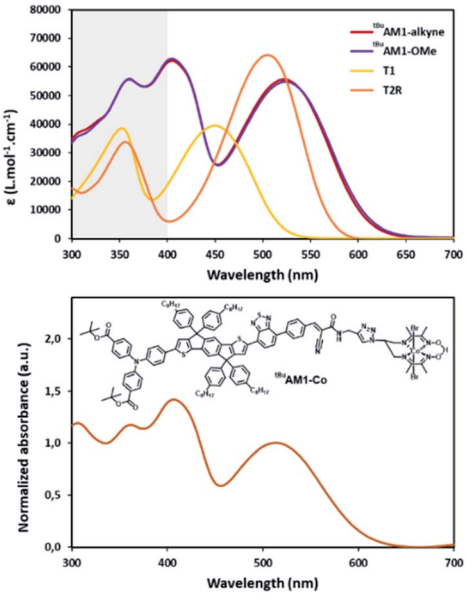

Fig. 3 UV-Vis spectra of dyes ^{tBu}AM1-alkyne, ^{tBu}AM1-OMe, ^{tBu}T1 and ^{tBu}T2R (top) and dyad ^{tBu}AM1-Co (bottom), recorded in DCM at 25 °C.

absorption band, the average absorption of the new dyes in the visible range is significantly higher when comparing to **^{tBu}T2R**, due to a shift of the spectra towards longer wavelengths.

Compared to the dye spectra, the **^{tBu}AM1-Co** dyad spectrum displays a small hypsochromic shift of the ICT band of around 10 nm. The new absorption peak observed at 310 nm corresponds to the absorption of the Co(DO)(DOH)pn moiety.[17]

To get more insights into the optoelectronic properties of the dyad, cyclic voltammetry (CV) experiments were carried out for the three new compounds. The CV measurements were performed in a solution of $n$$Bu_4NPF_6$ 0.1 M in DCM as electrolyte at 25 °C for the oxidation process and in a solution of $n$$Bu_4NPF_6$ 0.1 M in DMF as electrolyte at 25 °C for the reduction since the reduction processes appeared more reversible in this solvent. For the CV trace of the **^{tBu}AM1-Co** dyad (orange trace Fig. S9†), we observed two oxidation waves in the anodic region. The two oxidation waves at 0.29 V and 0.51 V *vs.* $Fc^{+/0}$ correspond to the oxidation of the donating segment as compared to the electrochemical signature of the dye **^{tBu}AM1-alkyne** (red trace Fig. S9†). In the cathodic regime, we observed three waves at −1.52 V, −1.12 V, and −0.73 V *vs.* $Fc^{+/0}$. By comparison with the **^{tBu}AM1-alkyne** trace the peak at −1.52 V can be attributed to the reduction of the acceptor moiety whereas the two other waves observed at −1.12 V and −0.73 V correspond to the redox couple Co(II)/Co(I) and Co(III)/Co(II) respectively.

These measurements confirm that the electronic and redox properties comply with the thermodynamic requirements for photoelectrochemical hydrogen production. Although the reduction of the catalytic center *via* photo-induced intramolecular electron transfer from the excited state of the dye cannot be excluded, it is more likely that this system follows a pathway similar to the one previously reported for the **T2R-Co** sensitized photocathode,[23] *i.e.* with an ultrafast hole injection into the valence band of NiO, followed by a thermally-activated electron transfer from the reduced dye to the catalytic center. The driving force for the former process is calculated to be −0.71 eV ($\Delta G_{inj} = e[E_{FB}(NiO) - E(Dye^{*/-})]$; with $E_{FB}(NiO)$ = +0.46 V *vs.* NHE at pH 5.5 (ref. 23) and $E(Dye^{*/-}) = E(Dye^{0/-}) + E_{0-0}$), and the two successive reductions of the cobalt center are thermodynamically allowed with driving forces of −1.00 and −0.64 eV, respectively (calculated as $\Delta G_1 = e[E(PS/PS^-) - E(Co(III)/Co(II))]$ and $\Delta G_2 = e[E(PS/PS^-) - E(Co(II)/Co(I))]$).

2.3 Preparation of mesoporous NiO and Li-doped NiO photocathodes

For the evaluation of the photoelectrochemical activity of the new molecular dyad, we prepared mesoporous NiO electrodes. Nickel oxide is a p-type semiconductor with a band gap energy estimated between 3.6–4.0 eV.[45] It has been the dominant p-type semiconducting material for the preparation of DSPEC photocathodes in the last years.[46] However, this semiconducting material presents some limitations related to its intrinsic low hole mobility.[47] Stoichiometric NiO is an insulator at room temperature; however, its resistivity decreases upon increasing the concentration of Ni^{3+} sites, or by doping with monovalent atoms such as lithium.[48] Therefore, to evaluate the performances of our dyad, we prepared and compared two types of

NiO films *i.e.* pristine ones and Li-doped ones. Four consecutive layers of a F108-containing sol–gel precursor solution (w/o 1.5 to 6 molar% LiCl) were deposited by spin-coating onto fluorine-doped tin oxide (FTO)-coated glass electrodes followed by sintering at 450 °C, according to our previously reported procedure.[17] Thicknesses varying from 0.8 to 1 μm were measured by cross-section scanning electron microscopy for non-doped as well as Li-doped NiO films (Fig. S11†). As previously reported,[46,48,49] adding lithium atoms in the p-type semiconductor results in an increase of the electronic conductivity of the mesoporous films (Table S2†). The conductivity increases from 4 S m^{-1} to 24 S m^{-1} for non-doped, and 1.5% Li-doped electrodes respectively and it reaches 58 S m^{-1} for the 3% Li-doped films. SEM-images reveal a very homogenous surface for the films with lithium-doping concentration up to 3%, but ditches start to appear in the surface at higher concentration. Besides, we noticed that the nanoparticles get larger with increasing doping concentrations (see Table S3 and Fig. S12†), which makes electrodes with 3% Li-doping less interesting for testing our molecule. Indeed, we observed a drop of more than 60% of the dyad loading when the size of the particles increases from around 15 nm to 20 nm. After the quantitative hydrolysis of the *tert*-butyl esters using trifluoroacetic acid in DCM at 25 °C (see Experimental section for details and characterization of **AM1-Co** and **AM1-OMe**), pristine NiO layers and 1.5% Li-doped NiO layers were sensitized by soaking them for 24 h in a 0.5 mM solution of **AM1-Co**. Films sensitized with **AM1-OMe** were also prepared for comparison purposes. The amount of dyad (or dye) loaded at the surface of the NiO electrodes was estimated by UV-Vis absorption spectroscopy after desorption of a freshly sensitized film using a phenylphosphonic acid solution.[50] We found an average **AM1-Co** loading of 3.4 ± 1.8 nmol cm^{-2} on pristine NiO electrodes and 1.2 ± 0.5 nmol cm^{-2} on 1.5% Li-doped NiO electrodes. The lower amount of dyad attached on Li-doped NiO electrodes is consistent with the formation of bigger NiO nanoparticles when Li is incorporated (Table S3†). Overall, the surface concentration of the dyad is in the lower average compared to the previously reported NiO photocathodes[23] but might be explained by the bulkiness of this new molecular dyad.

2.4 Photoelectrochemical performances

The photoelectrochemical activity of the different films was assessed in a three-electrode configuration setup. We used our previously reported standardized conditions,[23] *i.e.* working in a 0.1 M aqueous MES/NaCl buffer at pH 5.5, at an applied potential of +0.14 V *vs.* RHE (−0.4 V *vs.* Ag/AgCl). Water-filled filter and UV cut-off filter were used to eliminate infra-red ($\lambda > 800$ nm) and UV irradiations ($\lambda < 400$ nm), respectively, to ensure an irradiation under visible light only (0.65 sun; see ESI† for details). Chronoamperometric measurements were first recorded under chopped light irradiation to get some insight into the magnitude and shape of the photocurrents. When light is turned on, the NiO|**AM1-Co** photocathode develops a steady-state cathodic photocurrent that stabilizes at −7 μA cm^{-2} (red trace in Fig. 4, top). Importantly, no photocurrent is generated in the absence of a photoactive component (control experiment with a pristine NiO electrode, grey trace in Fig. 4, top) and a lower photocurrent density is recorded on a film sensitized by the **AM1-OMe** dye alone (purple trace in Fig. 4, top). The photoelectrochemical hydrogen production activity of **AM1-OMe** is likely due to the light-driven reduction of electrically disconnected NiO particles, forming Ni(0) catalytic sites as previously observed for a related push–pull dye sensitized NiO photocathode.[51]

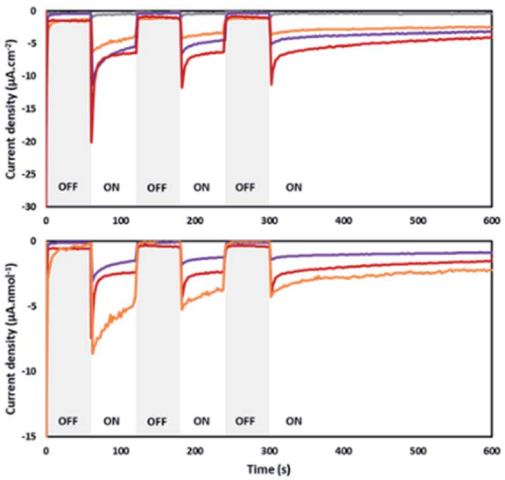

Fig. 4 Top: Chopped-light chronoamperometric measurements recorded at +0.14 V *vs.* RHE in 0.1 M aqueous MES/NaCl buffer pH 5.5 on a NiO (grey line), a NiO|**AM1-OMe** (purple line), a NiO|**AM1-Co** (red line) and a 1.5% Li–NiO|**AM1-Co** (orange line) photocathodes. Bottom: Normalized photocurrent densities related to the loading in photoactive component.

In order to provide a meaningful analysis of these data, the photocurrent density was normalized to the dyad/dye loading (Fig. 4, bottom); hence, a twice-higher photocurrent per nmol of photoactive component is generated when the cobalt catalyst is present at the surface of the film.

To confirm that a catalytic hydrogen production activity is at the origin of this photocurrent, two-hour chronoamperometric measurements were recorded under continuous irradiation (Fig. S13†) and the amount of H_2 produced during the course of the experiment was quantified by gas chromatography analysis of the headspace (Tables 2 and S4†). This allowed to determine a turnover number (TON) and a faradaic efficiency (F.E.) for

Table 2 Figures of merit determined from highest chronoamperometric measurements under continuous visible light irradiation. Additional measurements are available in Table S4 in ESI

	Dyad loading (nmol cm^{-2})	$n(H_2)$ (nmol)	TON	F.E. (%)
NiO|**T1-Co**[a]	8.2	5.8	<2	8
NiO|**T2R-Co**[a]	7.5	6.9	<2	12
NiO|**AM1-Co**[b]	3.0	86	30	16
1.5% Li–NiO|**AM1-Co**[b]	0.6	27	45	20

[a] Over 4 hours; value corresponding to the amount of H_2 measured in the headspace.[23] [b] Over 2 hours.

hydrogen production. Although standardized conditions were employed, a non-negligible dependence of the performances on the different batches of NiO films, their thicknesses or the dyad loading is observed (Table S4†). Nonetheless, compared to our previously reported systems NiO|**T1-Co** and NiO|**T2R-Co** assessed under identical conditions,[23] a significant increase in the performances is observed, in terms of both TON and F.E., more than doubled with **AM1-Co**. This result underlines that the cobalt-centered catalytic activity is not the kinetically limiting step in the process. Increasing the light harvesting efficiency of the dyad by introducing a IDT–BTD chromophore – and so, increasing the amount of photogenerated electrons – is clearly beneficial for the photoelectrochemical activity, as previously observed for a related photocathode based on a ruthenium trisdiimine photosensitizer coupled to Co(DO)(DOH)pn.[52] In addition, the presence of a bulky unit such as IDT in **AM1-Co** most likely contributes to better passivate the surface.[53]

Using 1.5% Li-doped NiO films might provide another track to improve the performances. Although the dyad loading on these films is currently low and needs to be improved, interesting features are observed: whereas photocurrent spikes are observed for the non-doped films when light is switched on, they are absent for the Li-doped ones and a photocurrent of higher intensity is recorded (normalized to the dyad loading in Fig. 4, bottom). This tends to indicate that, at the very beginning of the experiment (*i.e.* in the absence of any additional process that might alter the activity), the overall electron transfer kinetics is higher and charge accumulation at the electrode–electrolyte interface is avoided on the doped films, compared to the non-doped ones. The better electronic conductivity conferred by the doping most probably accounts for these effects, which translate into a higher TON value for hydrogen production (Tables 2 and S4†). Yet, after ten minutes, both films display almost similar photocurrent densities (per nmol of dyad) (Fig. 4 and S14†), suggesting that other processes might be taking over such as degradation processes. Of note, the bleaching of the **T2R** dye on the one hand and the hydrolysis of the Co(DO)(DOH)pn catalyst on the other hand were identified as two deactivation pathways in our previous studies.[23,52] Deciphering the parameters limiting the photoelectrochemical performances of NiO|**AM1-Co** and 1.5% Li–NiO|**AM1-Co** thanks to (post)operando investigations will therefore be the subject of future studies in order to develop devices that are more robust.

Conclusions

In conclusion, we synthesized and characterized a novel noble metal-free dye-catalyst assembly for hydrogen production in DSPECs. In this structure, the cobalt diimine dioxime catalyst is covalently coupled to a push–pull organic dye featuring a benzothiadiazole (BTD) unit; the latter is used to strengthen the push–pull effect within the dyad, thus enhancing the spatial charge separation upon visible light irradiation. The IDT unit extends the π-conjugation of the system which allows to extend the UV-absorption band towards the visible region. This molecular dyad, immobilized on mesoporous NiO electrodes, exhibits the highest photoelectrochemical hydrogen production activity of the series of structures based on the same catalyst and varying only by the nature of the π-conjugated spacer within the dye. The effects of lithium doping of the NiO electrodes were also investigated, and we show that Li-doped electrodes show a better electrical conductivity and increase the TON for hydrogen production of the system, supposedly by reducing the charge accumulation at the electrode–electrolyte interface. This work thus provides some guidelines to design efficient dye-catalyst assemblies for photoelectrochemical solar fuel production by a rational molecular engineering strategy. Combining the BTD-based dye **AM1-alkyne** with more robust cobalt catalysts[54,55] will be the next step to increase the photocathode activity and stability. Additionally, the implementation of a comprehensive (post)operando analysis will help establishing structure–activity relationships and will be instrumental to develop more efficient electrode materials.

Author contributions

AM synthesized and characterized the dyes and dyad, and carried out the photoelectrochemical measurements, EG contributed to the synthesis of the dyad, CA contributed to the supervision of the synthetic work, MB prepared and characterized the mesoporous NiO layers, JF contributed to the preparation of the NiO films, CSP and JP performed the MALDI-ToF-MS and ESI-MS analyses, PM and AM performed the quantum chemical calculations. RD, VA and MCK supervised the work, designed the materials and experiments, analysed the data.

Conflicts of interest

There are no conflicts to declare.

Acknowledgements

This work was supported by the French National Research Agency (Labex ARCANE, CBH-EUR-GS, ANR-17-EURE-0003) and the CEA through the DRF-Impulsion program. A. M. acknowledges CEA for funding through a CFR PhD grant. R. D. acknowledges the European Research Council (ERC) for funding. This work was partially funded under the European Union's Horizon 2020 Research and Innovation Programme (grant agreement number 832606; project PISCO). PM thanks GENCI (CINES and IDRIS) for HPC resources (Grant A0100807648). Dr B. Grévin is acknowledged for his assistance in the AFM studies of the electrodes, Dr S. Pouget is acknowledged for the X-ray diffraction analysis and Dr C. Cabanetos and Dr P. Blanchard for their help during the characterisation of the NiO layers.

Notes and references

1 M. K. Brennaman, R. J. Dillon, L. Alibabaei, M. K. Gish, C. J. Dares, D. L. Ashford, R. L. House, G. J. Meyer, J. M. Papanikolas and T. J. Meyer, *J. Am. Chem. Soc.*, 2016, **138**, 13085–13102.

2 P. Xu, N. S. McCool and T. E. Mallouk, *Nano Today*, 2017, **14**, 42–58.
3 K. Fan, F. Li, L. Wang, Q. Daniel, E. Gabrielsson and L. Sun, *Phys. Chem. Chem. Phys.*, 2014, **16**, 25234–25240.
4 F. Li, K. Fan, B. Xu, E. Gabrielsson, Q. Daniel, L. Li and L. Sun, *J. Am. Chem. Soc.*, 2015, **137**, 9153–9159.
5 S. Zhang, H. Ye, J. Hua and H. Tian, *EnergyChem*, 2019, **1**, 100015.
6 E. A. Gibson, *Chem. Soc. Rev.*, 2017, **46**, 6194–6209.
7 V. Nikolaou, A. Charisiadis, G. Charalambidis, A. G. Coutsolelos and F. Odobel, *J. Mater. Chem. A*, 2017, **5**, 21077–21113.
8 J. N. Clifford, E. Martínez-Ferrero, A. Viterisi and E. Palomares, *Chem. Soc. Rev.*, 2011, **40**, 1635–1646.
9 B. Shan, B. D. Sherman, C. M. Klug, A. Nayak, S. L. Marquard, Q. Liu, R. M. Bullock and T. J. Meyer, *J. Phys. Chem. Lett.*, 2017, **8**, 4374–4379.
10 A. Charisiadis, E. Giannoudis, Z. Pournara, A. Kosma, V. Nikolaou, G. Charalambidis, V. Artero, M. Chavarot-Kerlidou and A. G. Coutsolelos, *Eur. J. Inorg. Chem.*, 2021, **2021**, 1122–1129.
11 L. J. Antila, P. Ghamgosar, S. Maji, H. Tian, S. Ott and L. Hammarström, *ACS Energy Lett.*, 2016, **1**, 1106–1111.
12 C. E. Creissen, J. Warnan, D. Antón-García, Y. Farré, F. Odobel and E. Reisner, *ACS Catal.*, 2019, **9**, 9530–9538.
13 C. E. Creissen, J. Warnan and E. Reisner, *Chem. Sci.*, 2018, **9**, 1439–1447.
14 R. J. Kamire, M. B. Majewski, W. L. Hoffeditz, B. T. Phelan, O. K. Farha, J. T. Hupp and M. R. Wasielewski, *Chem. Sci.*, 2017, **8**, 541–549.
15 L. Li, L. Duan, F. Wen, C. Li, M. Wang, A. Hagfeldt and L. Sun, *Chem. Commun.*, 2012, **48**, 988–990.
16 L. Tong, A. Iwase, A. Nattestad, U. Bach, M. Weidelener, G. Götz, A. Mishra, P. Bäuerle, R. Amal, G. G. Wallace and A. J. Mozer, *Energy Environ. Sci.*, 2012, **5**, 9472.
17 N. Kaeffer, J. Massin, C. Lebrun, O. Renault, M. Chavarot-Kerlidou and V. Artero, *J. Am. Chem. Soc.*, 2016, **138**, 12308–12311.
18 K. A. Click, D. R. Beauchamp, Z. Huang, W. Chen and Y. Wu, *J. Am. Chem. Soc.*, 2016, **138**, 1174–1179.
19 P. B. Pati, L. Zhang, B. Philippe, R. Fernández-Terán, S. Ahmadi, L. Tian, H. Rensmo, L. Hammarström and H. Tian, *ChemSusChem*, 2017, **10**, 2480–2495.
20 N. Kaeffer, C. D. Windle, R. Brisse, C. Gablin, D. Leonard, B. Jousselme, M. Chavarot-Kerlidou and V. Artero, *Chem. Sci.*, 2018, **9**, 6721–6738.
21 C. D. Windle, H. Kumagai, M. Higashi, R. Brisse, S. Bold, B. Jousselme, M. Chavarot-Kerlidou, K. Maeda, R. Abe, O. Ishitani and V. Artero, *J. Am. Chem. Soc.*, 2019, **141**, 9593–9602.
22 K. L. Materna, A. M. Beiler, A. Thapper, S. Ott, H. Tian and L. Hammarström, *ACS Appl. Mater. Interfaces*, 2020, **12**, 31372–31381.
23 S. Bold, J. Massin, E. Giannoudis, M. Koepf, V. Artero, B. Dietzek and M. Chavarot-Kerlidou, *ACS Catal.*, 2021, **11**, 3662–3678.
24 F. Wu, J. Liu, X. Li, Q. Song, M. Wang, C. Zhong and L. Zhu, *Eur. J. Org. Chem.*, 2015, **2015**, 6850–6857.
25 J. V. S. Krishna, D. Koteshwar, T. H. Chowdhury, S. P. Singh, I. Bedja, A. Islam and L. Giribabu, *J. Mater. Chem. C*, 2019, **7**, 13594–13605.
26 H. Song, J. Zhang, J. Jin, H. Wang and Y. Xie, *J. Mater. Chem. C*, 2018, **6**, 3927–3936.
27 P. B. Pati, G. Damas, L. Tian, D. L. A. Fernandes, L. Zhang, I. B. Pehlivan, T. Edvinsson, C. M. Araujo and H. Tian, *Energy Environ. Sci.*, 2017, **10**, 1372–1376.
28 J. Warnan and E. Reisner, *Angew. Chem., Int. Ed.*, 2020, **59**, 17344–17354.
29 A. B. Muñoz-García, I. Benesperi, G. Boschloo, J. J. Concepcion, J. H. Delcamp, E. A. Gibson, G. J. Meyer, M. Pavone, H. Pettersson, A. Hagfeldt and M. Freitag, *Chem. Soc. Rev.*, 2021, **50**, 12450–12550.
30 M. Bartolini, V. Gombac, A. Sinicropi, G. Reginato, A. Dessì, A. Mordini, J. Filippi, T. Montini, M. Calamante, P. Fornasiero and L. Zani, *ACS Appl. Energy Mater.*, 2020, **3**, 8912–8928.
31 L. Nhon, B. Shan, A. D. Taggart, R. M. W. Wolfe, T.-T. Li, C. M. Klug, A. Nayak, R. M. Bullock, J. F. Cahoon, T. J. Meyer, K. S. Schanze and J. R. Reynolds, *ACS Appl. Mater. Interfaces*, 2021, **13**, 47499–47510.
32 M. Godfroy, J. Liotier, V. M. Mwalukuku, D. Joly, Q. Huaulmé, L. Cabau, C. Aumaitre, Y. Kervella, S. Narbey, F. Oswald, E. Palomares, C. A. González Flores, G. Oskam and R. Demadrille, *Sustainable Energy Fuels*, 2021, **5**, 144–153.
33 S. Karamshuk, S. Caramori, N. Manfredi, M. Salamone, R. Ruffo, S. Carli, C. Bignozzi and A. Abbotto, *Energies*, 2016, **9**, 33.
34 D. Joly, M. Godfroy, L. Pellejà, Y. Kervella, P. Maldivi, S. Narbey, F. Oswald, E. Palomares and R. Demadrille, *J. Mater. Chem. A*, 2017, **5**, 6122–6130.
35 H. Chen, Y. Gong, Á. Vázquez-Mayagoitia, J. Zhang and J. M. Cole, *ACS Appl. Energy Mater.*, 2020, **3**, 423–430.
36 Q. Tao, M. Xiao, M. Zhu, L. Shao, Z. Sui, P. Wang, G. Huang, Y. Pei, W. Zhu and F. Huang, *Dyes Pigm.*, 2017, **144**, 142–150.
37 ADF SCM, *Theoretical Chemistry*, Vrije Universiteit, Amsterdam, The Netherlands, **https://www.scm.com**.
38 G. te Velde, F. M. Bickelhaupt, E. J. Baerends, C. Fonseca Guerra, S. J. A. van Gisbergen, J. G. Snijders and T. Ziegler, *J. Comput. Chem.*, 2001, **22**, 931–967.
39 S.-H. Chan, C.-P. Chen, T.-C. Chao, C. Ting, C.-S. Lin and B.-T. Ko, *Macromolecules*, 2008, **41**, 5519–5526.
40 D. Joly, L. Pellejà, S. Narbey, F. Oswald, J. Chiron, J. N. Clifford, E. Palomares and R. Demadrille, *Sci. Rep.*, 2015, **4**, 4033.
41 C.-H. Chang, Y.-C. Chen, C.-Y. Hsu, H.-H. Chou and J. T. Lin, *Org. Lett.*, 2012, **14**, 4726–4729.
42 N. Yu. Gorobets, B. H. Yousefi, F. Belaj and C. O. Kappe, *Tetrahedron*, 2004, **60**, 8633–8644.
43 S. Bold, L. Zedler, Y. Zhang, J. Massin, V. Artero, M. Chavarot-Kerlidou and B. Dietzek, *Chem. Commun.*, 2018, **54**, 10594–10597.

44 S. Bold, T. Straistari, A. B. Muñoz-García, M. Pavone, V. Artero, M. Chavarot-Kerlidou and B. Dietzek, *Catalysts*, 2020, **10**, 1340.
45 H. Sato, T. Minami, S. Takata and T. Yamada, *Thin Solid Films*, 1993, **236**, 27–31.
46 C. J. Wood, G. H. Summers, C. A. Clark, N. Kaeffer, M. Braeutigam, L. R. Carbone, L. D'Amario, K. Fan, Y. Farré, S. Narbey, F. Oswald, L. A. Stevens, C. D. J. Parmenter, M. W. Fay, A. La Torre, C. E. Snape, B. Dietzek, D. Dini, L. Hammarström, Y. Pellegrin, F. Odobel, L. Sun, V. Artero and E. A. Gibson, *Phys. Chem. Chem. Phys.*, 2016, **18**, 10727–10738.
47 S. Wrede and H. Tian, *Phys. Chem. Chem. Phys.*, 2020, **22**, 13850–13861.
48 T. Dutta, P. Gupta, A. Gupta and J. Narayan, *J. Appl. Phys.*, 2010, **108**, 083715.
49 H.-T. Wang, D. K. Mishra, P. Chen and J.-M. Ting, *J. Alloys Compd.*, 2014, **584**, 142–147.
50 D. Ameline, S. Diring, Y. Farre, Y. Pellegrin, G. Naponiello, E. Blart, B. Charrier, D. Dini, D. Jacquemin and F. Odobel, *RSC Adv.*, 2015, **5**, 85530–85539.
51 D. A. Hoogeveen, M. Fournier, S. A. Bonke, A. Nattestad, A. Mishra, P. Bäuerle, L. Spiccia, A. J. Mozer and A. N. Simonov, *J. Phys. Chem. C*, 2017, **121**, 25836–25846.
52 E. Giannoudis, S. Bold, C. Müller, A. Schwab, J. Bruhnke, N. Queyriaux, C. Gablin, D. Leonard, C. Saint-Pierre, D. Gasparutto, D. Aldakov, S. Kupfer, V. Artero, B. Dietzek and M. Chavarot-Kerlidou, *ACS Appl. Mater. Interfaces*, 2021, **13**, 49802–49815.
53 H.-L. Jia, M.-D. Zhang, W. Yan, X.-H. Ju and H.-G. Zheng, *J. Mater. Chem. A*, 2016, **4**, 11782–11788.
54 N. Queyriaux, R. T. Jane, J. Massin, V. Artero and M. Chavarot-Kerlidou, *Coord. Chem. Rev.*, 2015, **304–305**, 3–19.
55 L. Tong, L. Duan, A. Zhou and R. P. Thummel, *Coord. Chem. Rev.*, 2020, **402**, 213079.

